Bulletin of the Seismological Society of America, Vol. 105, No. 6, pp. 3068–3082, December 2015, doi: 10.1785/0120150100

Rupture Directivity from Strong-Motion Recordings of the 2013 Lushan Aftershocks

by Ruizhi Wen, Hongwei Wang, and Yefei Ren

Abstract The observed directivity effects of ground motion have extensive implications for both earthquake source physics and earthquake-hazard analyses on active fault zones. In general, it is still difficult to determine the rupture directivity in detail for smaller earthquakes because of limited azimuthal coverage. Four Lushan aftershocks that occurred on 20 and 21 April 2013 (events I, II, III, and IV) were well recorded by the National Strong-Motion Observation Network System of China. An interesting phenomenon was clearly observed: the distributions of the triggered stations for the four aftershocks, which had adjacent hypocenters and similar magnitudes, differed significantly from each other. The analyses of ground-motion parameters, including the peak ground-motion parameters, response spectra, and durations, indicate that the directivity of the ground motion was significant for events II and III. The Fourier spectral ratio method was used to imprint the rupture directivity. We calculated the rupture direction and rupture velocity by inverting the peak parameters. Random realizations in many times were utilized to consider the uncertainty in the results of the inversion. The results indicate that the four events shared the similar northeast–southwest-trending fault plane and had similar rupture velocities of approximately 2.1 km/s. Event I was more likely to be a perfectly symmetric bilateral rupture, though there was large uncertainty in the results of the inversion. The rupture for events II and III propagated predominantly toward the southwest. However, event IV was observed to have an approximately symmetric bilateral propagation, slightly inclining to the northeast. We also confirmed the period-dependent directivity effect by inverting the response spectra at different periods.

Introduction

Source rupture direction, which has a strong influence on the spatial pattern of the ground motion, is related to the earthquake disaster. The evaluation of source rupture characteristics is of considerable significance for seismic-hazard emergency management, including the rapid reporting of seismic intensity, seismic loss assessment, and postearthquake emergency management. Fault rupture ambiguity is generally resolved using basic prior knowledge of active fault orientation, historical earthquakes, distribution of aftershocks, and observed surface rupture.

The predominance of unilateral ruptures in large earthquakes was verified by McGuire *et al.* (2002). When a rupture propagates predominantly in a single direction from nucleation, the resulting ground motion can be subjected to a dramatic azimuthal effect, which is commonly referred to as the directivity effect. It induces more severe ground motion in the direction of the predominant rupture, which is characterized by higher amplitudes and shorter durations. Significant directivity effects have been recognized in large numbers of destructive earthquakes, including the 28 June 1992 M_w 7.3 Landers, California, earthquake (Velasco *et al.*, 1994), the 17 January 1994 M_w 6.7 Northridge, California, earthquake (Somerville *et al.*, 1996), the 17 January 1995 M_w 6.9 Kobe, Japan, earthquake (Somerville *et al.*, 1996), the 21 September 1999 M_w 7.7 Chi-Chi, Taiwan, earthquake (Phung *et al.*, 2004), and the 12 May 2008 M_w 7.8 Wenchuan, Sichuan, earthquake (Hu and Xie, 2011).

Because of insufficient seismic data resolution and azimuthal coverage, exact observation of the directivity effect of small-to-moderate earthquakes is limited (Kane *et al.*, 2013). For a moderate earthquake, the source is usually assumed to be a simple circular homogeneous rupture without allowing for the complexity of the rupture. However, rupture directivity relative to smaller earthquakes has been widely demonstrated in the literature using different methods. Boatwright and Boore (1982) studied the strong-motion accelerograph recordings of the M_w 5.8 Livermore Valley, California, mainshock and the M_w 5.4 largest aftershock in 1980 and attributed the systematic variations of the peak ground acceleration (PGA) and peak ground velocity (PGV) with azimuth or station location to the source directivity. López-Comino *et al.* (2012) investigated the apparent source time functions based on the empirical Green's function deconvolution technique and the distribution of aftershocks to reveal a clear rupture directivity for the M_w 5.2 Lorca earthquake in southeast Spain. Mori (1996), Lanza *et al.* (1999), McGuire (2004), and Tan and Helmberger (2010) also confirmed rupture directivities of smaller earthquakes by azimuthal apparent source durations. Kane *et al.* (2013) used a simple comparison of displacement spectra to estimate rupture directivity of 450 small earthquakes at Parkfield along the San Andreas fault.

In recent years, Boatwright (2007) and Seekins and Boatwright (2010) derived an inversion of the peak parameters of ground motion to determine rupture direction and rupture velocity of moderate earthquakes and tested the results of the inversion. Convertito *et al.* (2012) and Convertito and Emolo (2012) extended this method to allow for rapid retrieval of the surface fault projection and dominant rupture direction for moderate-to-large earthquakes. The outstanding merit of this method is that only magnitude estimation, hypocentral location, and peak parameters of ground motion are needed to evaluate rupture directivity.

On 20 April 2013, at 08:02 a.m. Beijing time, a strong earthquake hit Lushan, a county in the southwest of the Sichuan Province in China. This earthquake sequence fell within the National Strong-Motion Observation Network System (NSMONS), and many strong-motion stations were triggered—not only by the mainshock, but also by the aftershocks (Wen and Ren, 2014). Although the Lushan mainshock did not show a dominant rupture direction (Zhang *et al.*, 2013), the large number of recordings of the Lushan aftershocks met the engineering requirements for determining the directivity effect of smaller earthquakes.

In this article, we selected four groups of strong-motion recordings from four magnitude M 5.4 Lushan aftershocks and analyzed three basic engineering parameters, including the peak ground-motion parameter, response spectrum, and duration, to determine the directivity effect of ground motion. We then confirmed that the rupture directivity was the main cause of the directivity effect of ground motion based on the Fourier spectral ratio. Finally, we inverted the peak parameters to determine the main source rupture parameters, that is, the rupture direction and rupture velocity.

Lushan Earthquake Sequence

The Lushan earthquake occurred between the Pengguan fault and the Dayi fault on the northeast-trending Longmen Shan fault system (LFS; Han *et al.*, 2014). The LFS lies along the eastern margin of the Tibetan plateau as a result of crustal extrusion against the strong lithosphere of the Sichuan basin, which is a part of the Yangtze block. The epicenter distance was approximately 70 km between the Lushan earthquake and the Wenchuan M_s 8.0 earthquake that occurred on 12 May 2008. The rupture process of the Lushan earthquake was inverted by Wang *et al.* (2013) using regional broadband waveforms; their results indicated that the calculated moment magnitude M_w was 6.7, and the strike, dip, and rake angles were 205°, 38.5°, and 88.8°, respectively. These solutions confirmed that the Lushan earthquake was a thrust event. The mainshock did not have a significantly predominant rupture direction (Zhang and Lei, 2013). Following the mainshock, approximately 3000 aftershocks occurred within three days in an area of 45 km × 20 km that was located in Baoxing, Qionglai, Lushan, and Tianquan Counties (Liu *et al.*, 2013), which was consistent with the above-mentioned fault rupture plane determined by Wang *et al.* (2013). Most of the aftershocks were characterized by northwest-dipping faulting mechanisms (Zhang and Lei, 2013).

NSMONS aims to enhance earthquake monitoring and the collection of strong-motion recordings in earthquake-prone regions and in some major cities in the Chinese mainland. It has a higher density around the eastern-southeastern margin of the Tibetan plateau, and the earthquake sequence after the M_s 8.0 Wenchuan earthquake was also well recorded by NSMONS (Li *et al.*, 2008). For the Lushan earthquake sequence, up to 6 July 2013, there were a total of 1123 strong-motion recordings from NSMONS, including recordings from seven temporal strong-motion stations. Figure 1 shows the strong-motion stations that were triggered in the mainshock. The stations were generally distributed on the edge of the Sichuan basin or along the LFS and the Anninghe–Zemuhe fault zone (AZFZ). Most of the NSMONS stations in this region were triggered by the mainshock and the following aftershocks. We inferred that the NSMONS performed well in the Lushan earthquake sequence. Meanwhile, there was no visible directivity based on the spatial distributions of the triggered strong-motion stations.

There were only four aftershocks of $M > 5.0$ (events I, II, III, and IV) in the Lushan earthquake sequence (Table 1). All four aftershocks were M 5.4, as determined by the China Earthquake Network Center, and the focal mechanisms of the last three events in the Global Centroid Moment Tensor (Global CMT) catalog were approximately the same, though they had different moment magnitudes. Figure 2 shows the locations of the strong-motion stations that were triggered during each of the four aftershocks. Most of the triggered stations for the four aftershocks were within $a \pm 45°$ window of the LFS trace or the strike of the mainshock. Interestingly, it can be clearly observed that the distribution of the triggered stations in the four aftershocks with adjacent hypocenters was significantly different.

Event I only triggered 32 strong-motion stations, which were almost uniformly distributed from northeast to southwest. Fewer stations were triggered than expected, because there were fewer triggered stations within or near the surface fault projection. The reason for this could be that NSMONS is not a real-time data-stream system, and the strong-motion data are usually stored on removable memory cards. Event I occurred only ~5 min after the mainshock, and the instruments may not have recovered or the postevent data processing may not have detected the aftershock. Event II triggered 53 strong-motion stations that were evenly distributed along the fault strike of the mainshock. Likewise,

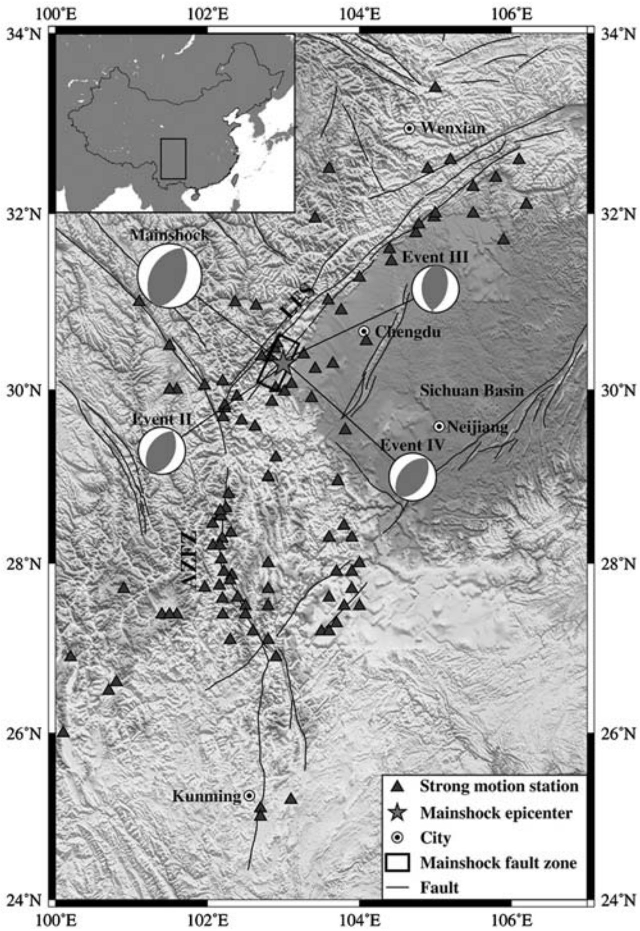

Figure 1. Triggered strong-motion stations during the Lushan mainshock. Some of the stations that were triggered in the Weihe basin, Shanxi Province, were not included because of the large epicentral distance. The surface fault projection of the fault plane was inverted by Wang *et al.* (2013). The focal mechanisms were derived from the Global Centroid Moment Tensor (Global CMT) catalog, except for that of event I. The inset map indicates the location of the study area. AZFZ is the Anninghe–Zemuhe fault zone.

53 strong-motion stations were triggered by event III, but the overwhelming majority was located to the southwest–southeast of the epicenter. Event IV triggered 52 strong-motion stations, and most of the stations were distributed to the northeast, which was opposite to event III. It appears that the four aftershocks that had similar magnitudes and adjacent hypocenters had different directivities.

Directivity Effect of Strong Ground Motion

Data Processing

The strong-motion recordings of the four aftershocks were uniformly processed using the same methodology that we used for the Wenchuan earthquake (Boore, 2001; Ren *et al.*, 2011). As a result, the processed ground motions can be used to provide reliable estimations of the PGA, PGV, and spectral ordinates that are of interest to engineers. To more obviously reflect the directivity effect of the strong ground motion, we rotated the two horizontal components (east–west [EW] and north–south [NS]) to the strike-normal (NF) and strike-parallel (PF) directions using the strike of the mainshock as inverted by Wang *et al.* (2013). Although the strikes of the four events were different from the mainshock, it is feasible to rotate all of the recordings of the four aftershocks following the fault strike for the purpose of clearly demonstrating the directivity effects instead of the precise rotated ground motions.

Peak Ground-Motion Parameters

The contour maps of the geometric means of the PGAs of the two orthogonal horizontal components for the four events were interpolated using the kriging interpolation method (Matheron, 1973), as shown in Figure 2. Significant differences among the PGA contour maps of the four events were observed. Contour maps of the four events were elongated to the northeast and/or the southwest. We simply defined an individual strike-normal line for each event perpendicular to the strike of the mainshock and crossed the epicenter of each event to divide the strong-motion stations into two groups, that is, the northeastern group (NEG) and the southwestern group (SWG), as shown in Figure 2. The PGA contours for event I have an approximate axial symmetry disposed about the strike-normal direction. Although it appears that event II triggered a similar number of stations in the NEG and the SWG, stations that were far from the epicenter in the NEG experienced smaller PGAs, which did not exceed 5 cm/s^2. The con-

Table 1
Basic Seismic Parameters of the Lushan Mainshock and the Four Aftershocks

Event Name	Date (yyyy/mm/dd)	Time (Beijing Time, hh:mm:ss)	Latitude (° N)	Longitude (° E)	Focal Depth (km)	M	M_W	First Nodal Plane (Strike/Dip/Rake) (°)	Second Nodal Plane (Strike/Dip/Rake) (°)
Mainshock	2013/04/20	08:02:46	30.30	103.00	13.0	7.0	6.6	212/42/100	19/49/81
							6.7*	205.0/38.5/88.0*	26.5/51.5/91.2*
Event I	2013/04/20	08:07:30	30.32	102.92	10.0	5.4	-	-	-
Event II	2013/04/20	11:34:17	30.24	102.94	15.0	5.4	5.4	215/45/100	21/46/80
Event III	2013/04/21	04:53:44	30.36	103.05	27.0	5.4	4.8	177/42/74	17/50/103
Event IV	2013/04/21	17:05:24	30.34	103.00	17.0	5.4	5.2	221/45/94	35/45/86

*Focal mechanisms that were inverted by Wang *et al.* (2013).

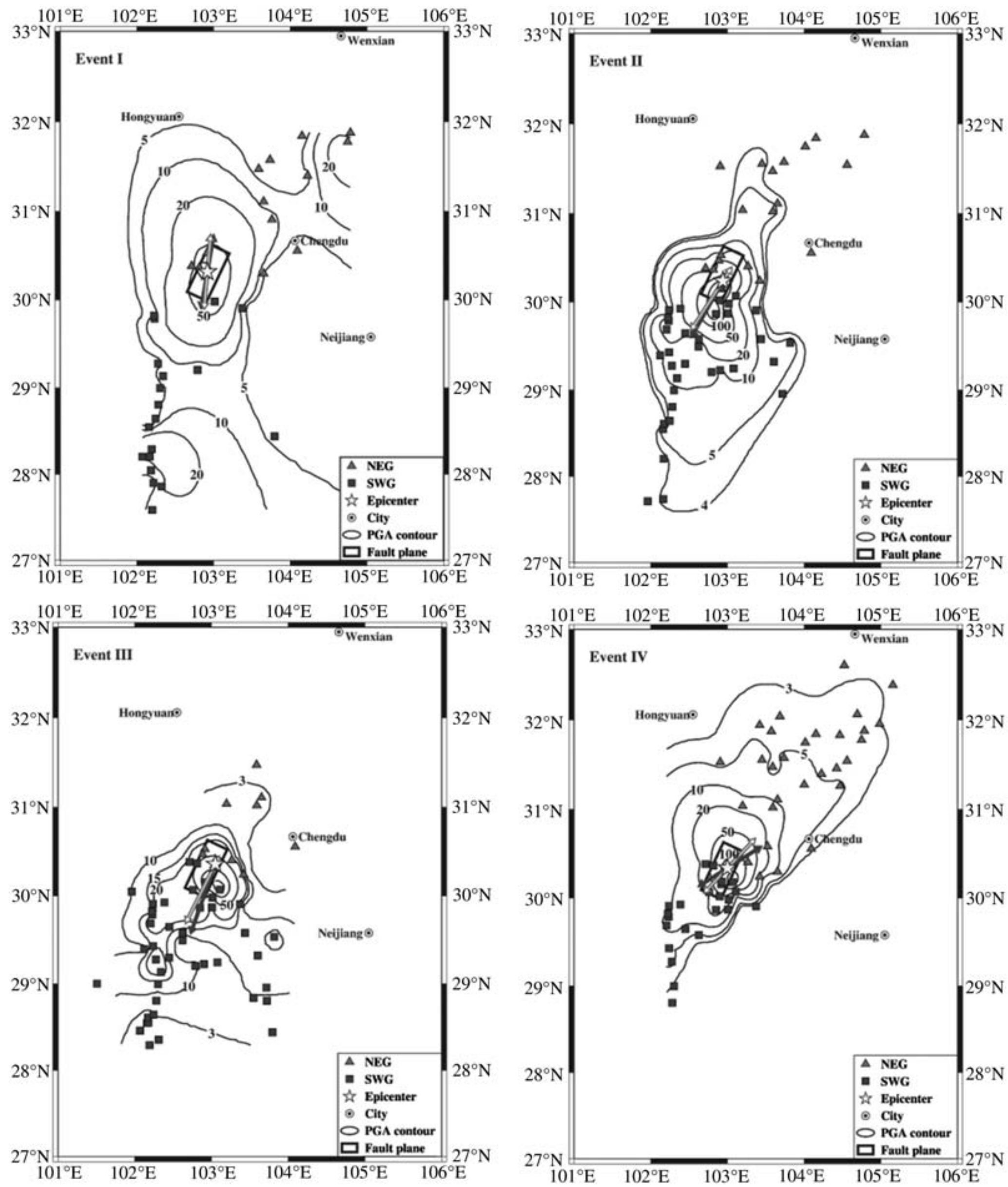

Figure 2. Triggered strong-motion stations for the four Lushan aftershocks and peak ground acceleration (PGA) contour maps. The event name is shown on the upper-left corner of each panel. The rectangular frame represents the surface fault projection of the mainshock that was inverted by Wang *et al.* (2013). The Arabic numbers represent the PGA values in centimeters per square second. The hollow and solid arrows represent the rupture directions that were inverted by the PGA and peak ground velocity (PGV), respectively. The lengths of the arrows represent the rupture proportion and are not the actual rupture lengths in the respective directions. The strong-motion stations are shown as two groups, the northeastern group (NEG, triangles) and the southwestern group (SWG, squares).

tours indicate that the PGA attenuated more slowly in the southwest. The contours for event III were not as clear as those for event II, but the attenuation characteristics were similar to that of event II, that is, the attenuation was slower in the southwest. In contrast to the three earlier events, the PGAs for event IV with hypocenter distances (R_{hyp}) less than 150 km had similar attenuation trends with distance in the NEG and the SWG, but the attenuation gradually diminished to the northeast as the distance increased. The PGV contour maps were also calculated like the PGA contour maps. All of the PGV and PGA contour maps for the four events had similar trends.

Response Spectra

We adopted a simple comparison of the 5% damped pseudospectral acceleration (PSA), as well as the average spectral ratio between the SWG and NEG to present the directivity effect, as shown in Figure 3. The average spectral ratio was defined as the ratio of the average PSAs of the strong-motion

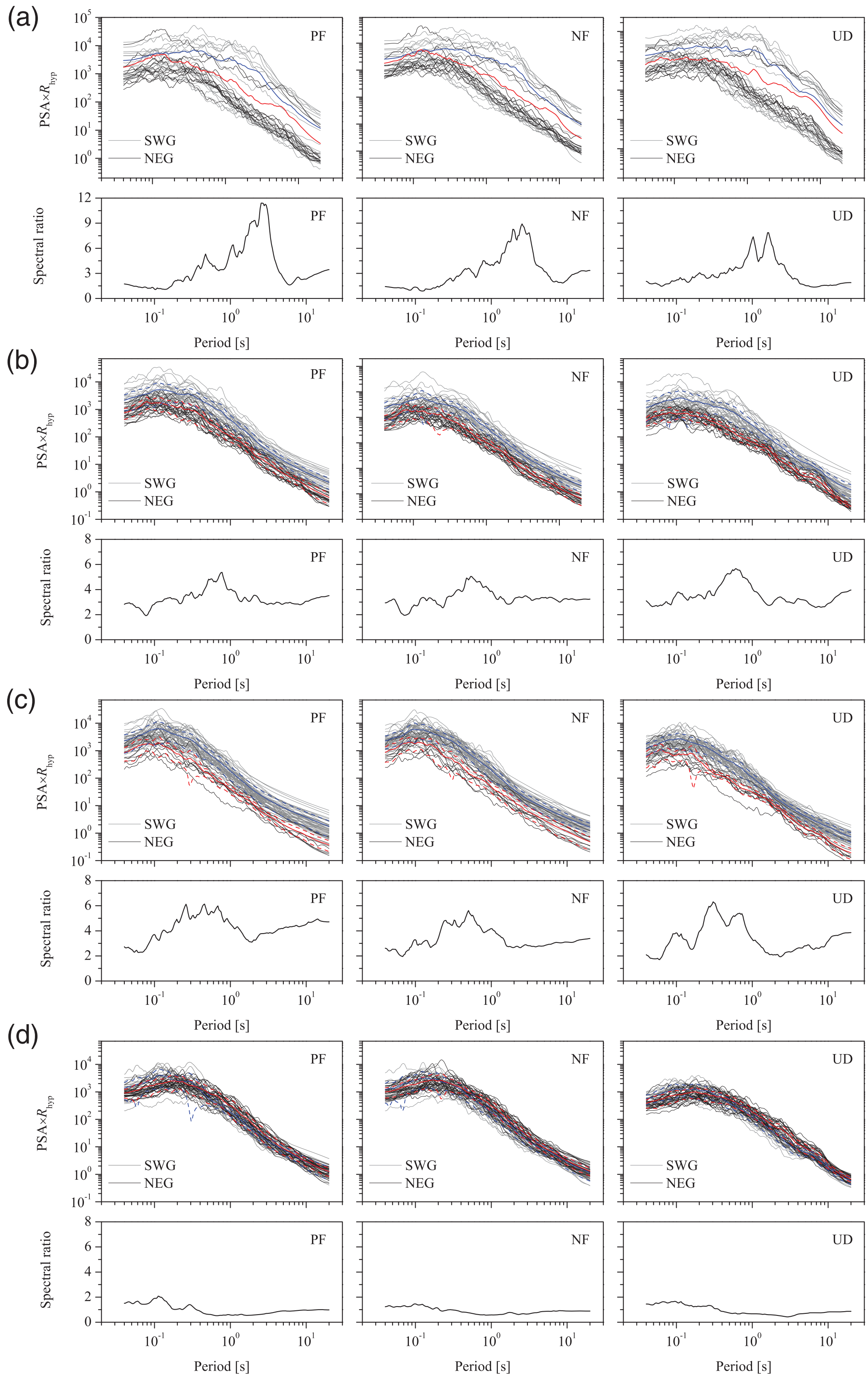

Figure 3. Comparison of the pseudospectral accelerations (PSAs) normalized by the hypocenter distance, as well as the average spectral ratio between the SWG and the NEG for (a) event I, (b) event II, (c) event III, and (d) event IV. PF, NF, and UD represent the strike-parallel, strike-normal, and up-down components of strong-motion recordings, respectively. The red and blue solid lines represent the average of the spectra in the NEG and SWG, respectively. The dashed line is the average ± 1standard deviation.

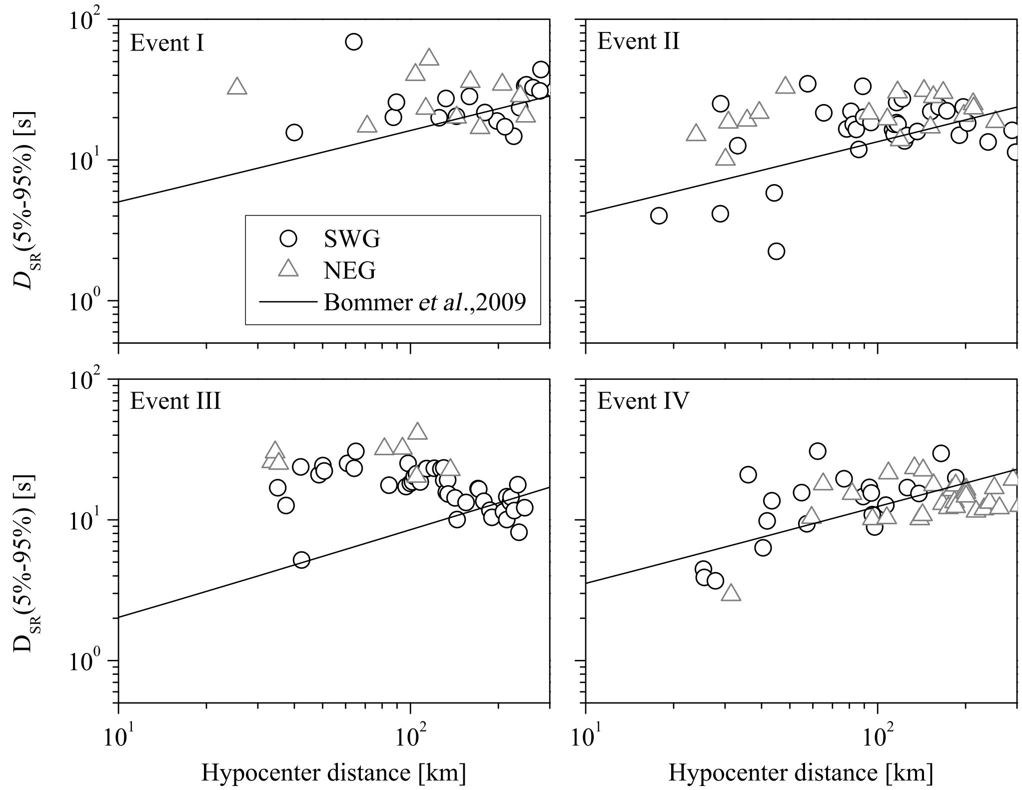

Figure 4. Comparison of the observed values of the geometric mean of D_{SR} (5%–95%) of the two orthogonal horizontal components with the empirical prediction of Bommer *et al.* (2009).

recordings in the SWG to that in the NEG. To remove the effect of geometrical spreading on the strong motion, we multiplied the PSA by the hypocenter distance. The corrected PSAs (PSA × R_{hyp}) of strong-motion recordings for event I in the NEG and SWG intermingle with each other, but PSAs of some strong-motion recordings far away from the epicenter (> 200 km), both in the NEG and SWG, are much higher than the others. The average spectral ratios are much higher, and a peak about 10.0 at intermediate periods occurs. This phenomenon may be ascribed to the fewer strong-motion recordings in the near field and the extraordinarily high strong-motion recordings in the far field (as shown in Fig. 2) but not to factors related to the directivity. For events II and III, a visible separation is seen between the SWG and the NEG, and the PSAs in the SWG are considerably higher than those in the NEG. The average spectral ratios at the whole periods are not less than 1.5, and the maximum value approaches approximately 6.0. It is worth noting that a single peak appears at intermediate periods (approximately 0.5–1.0 s). For event IV, closely parallel PSAs from the two groups can be observed, and the average spectral ratio is approximately 1.0.

Durations

The strong-motion duration is the sum of the path-dependent duration and the source duration that is related to the source rupture process. We did not focus on the path-dependent duration for the purpose of determining the directivity effect; rather we compared the geometric means of the significant duration D_{SR} (5%–95%) of the two orthogonal horizontal components with an empirical predictive equation that was developed by Bommer *et al.* (2009), as shown in Figure 4.

The rupture radii of the four analyzed events were approximately 2.7–5.3 km, according to the relationship between the moment magnitude and the rupture area (Somerville *et al.*, 1999). Except for one recording obtained in event II, the hypocenter distances of the other recordings were greater than 20 km, which is far more than the rupture radius. Therefore, the hypocenter distance could be regarded as an approximate substitute for the rupture distance in equation (5) of Bommer *et al.* (2009). The comparison shows that the empirical prediction significantly underestimated the observed values with $R_{hyp} \leq 100$ km. For event I, the durations at the SWG sites were approximately the same as the durations at the NEG sites. For events II and III in general, the sites in the NEG experienced durations that were longer than the durations at sites with the similar hypocenter distance in the SWG, especially at short distances. Approximately identical durations can be observed with $R_{hyp} > 100$ km for both groups for event IV, but we observed that sites with small distances in the SWG were exposed to prolonged shaking time.

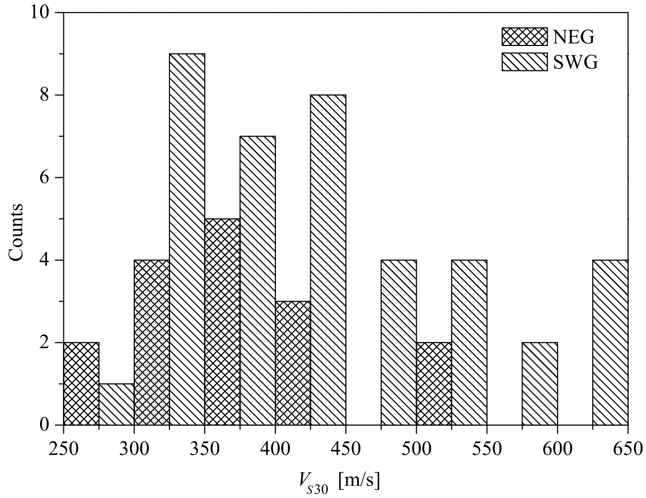

Figure 5. Comparison of V_{S30} for the NEG and SWG.

Confirmation of Rupture Directivity

According to the observed strong-motion parameters that were mentioned previously, it appears that a directivity effect could exist for events II and III, given the discrepancy in characteristics of the strong-motion recordings in the NEG and SWG. The observed directivity effect may be ascribed to one or more causes that are described below, that is, source rupture directivity, radiation pattern, local site condition, and attenuation characteristics of the propagation medium.

The average shear-wave velocity in the uppermost 30 m (V_{S30}) generally represents the local site conditions. Figure 5 presents a histogram of the distribution of V_{S30} for strong-motion stations in the NEG and SWG. V_{S30} was derived from the Next Generation Attenuation (NGA) site database (see Data and Resources). The V_{S30} of the majority of the NEG sites varies within a small range from 300 to 450 m/s; the average is 379.8 m/s. Although a few SWG sites have V_{S30} that is greater than 500 m/s; the average V_{S30} of the SWG sites is 431.7 m/s, which is slightly larger than that in the NEG. It is possible to assign a single V_{S30} to all of the sites, and the differences in local site effects on strong motion can be reasonably neglected. The results of the previous study indicated that the attenuation of the propagation medium on seismic waves, which was measured using the quality factor (Q), was almost same in the NEG and SWG regions (Ma *et al.*, 2007; Wang *et al.*, 2008).

After removing the interference of the site and propagation medium, it can be inferred that source directivity (rupture directivity and/or radiation pattern) causes the directivity effect on the observed strong ground motion. Spectral ratio analysis is a convenient approach for eliminating the effects of the site and propagation path on strong ground motion and to extract only the source effect. Provided that the distance between two events (events 1 and 2) is much smaller than the hypocenter distances from a common site (j) to both events, the Fourier spectral ratio of the two events recorded at the same site can be represented as

$$\frac{O_{1j}}{O_{2j}} = \frac{S_1(f)G_j(f)P_{1j}(f)}{S_2(f)G_j(f)P_{2j}(f)} \approx \frac{S_1(f)}{S_2(f)}, \tag{1}$$

in which $O(f)$, $S(f)$, $G(f)$, and $P(f)$ represent the observed S-wave Fourier spectrum, the source spectrum, the site amplification factor, and the propagation path effect, respectively, and f is the frequency. $P_{1j}(f) = P_{2j}(f)$ can be assumed because the two propagation paths are almost uniform. Therefore, $O_{1j}(f)/O_{2j}(f)$ is expected to be $S_1(f)/S_2(f)$. At all of the sites, the observed variations in $O_{1j}(f)/O_{2j}(f)$ are expected to be quite small if the two events have similar source directivity.

Figure 6 shows the Fourier spectral ratios, O_{1j}/O_{2j}, and the standard deviations of $\log_{10}(O_{1j}/O_{2j})$ from three pairs of events (event II/III, event II/IV, and event IV/III). The standard deviation of $\log_{10}(O_{1j}/O_{2j})$ is a measure of the amount of the dispersion of the logarithm (base 10) of the Fourier spectral ratios. Recordings with $R_{\rm hyp} \le 50$ km were excluded to reduce the effect of uncertainties of the distances. The spectral ratios for the three components of the strong-motion recordings have similar trends. The event II/III pair shows that sites in the NEG and SWG had constant spectral ratios, which were almost independent of the site location as expected, and the standard deviation of $\log_{10}(O_{1j}/O_{2j})$ was small (approximately 0.2) and smoothly varies, except at lower frequencies (<0.2 Hz). The event II/IV and event IV/III pairs performed similarly to one another and had large variations that were highly dependent on the site location, especially at intermediate frequencies of approximately 1.0–2.0 Hz. A single peak can be observed in the standard deviation of $\log_{10}(O_{1j}/O_{2j})$, and the maximum value is approximately 0.6. These results reveal that events II and III had exceptionally consistent source directivity but were distinct from that of event IV.

It is possible to employ the variation of the spectral ratio with azimuth to determine whether the source rupture directivity and/or the radiation pattern result in the source directivity (Hoshiba, 2003). Figure 7 shows the variations of spectral ratios with azimuth at different frequencies for event II/IV and event IV/III pairs. The amplitudes of the spectral ratios with azimuth at different frequencies have significant differences, but consistent variation tendencies can be observed, which is characterized by an obvious single peak or trough at approximately N200°E. We also calculated the radiation pattern ratios for event II/IV and event IV/III pairs (Fig. 7). The radiation pattern for the vector composition of the *SH* and *SV* components was obtained from the focal mechanism in Table 1, while the take-off angle was calculated using the 1D velocity model of the Longmen Shan region proposed by Zheng *et al.* (2009). The radiation pattern ratios of the event II/IV pair have slight variations with azimuth, and a trough appears at approximately 200°, which was not consistent with the variation tendency of the spectral ratios. A trough around 210° was observed both in the spectral ratios and in the radiation pattern ratios of the event IV/III

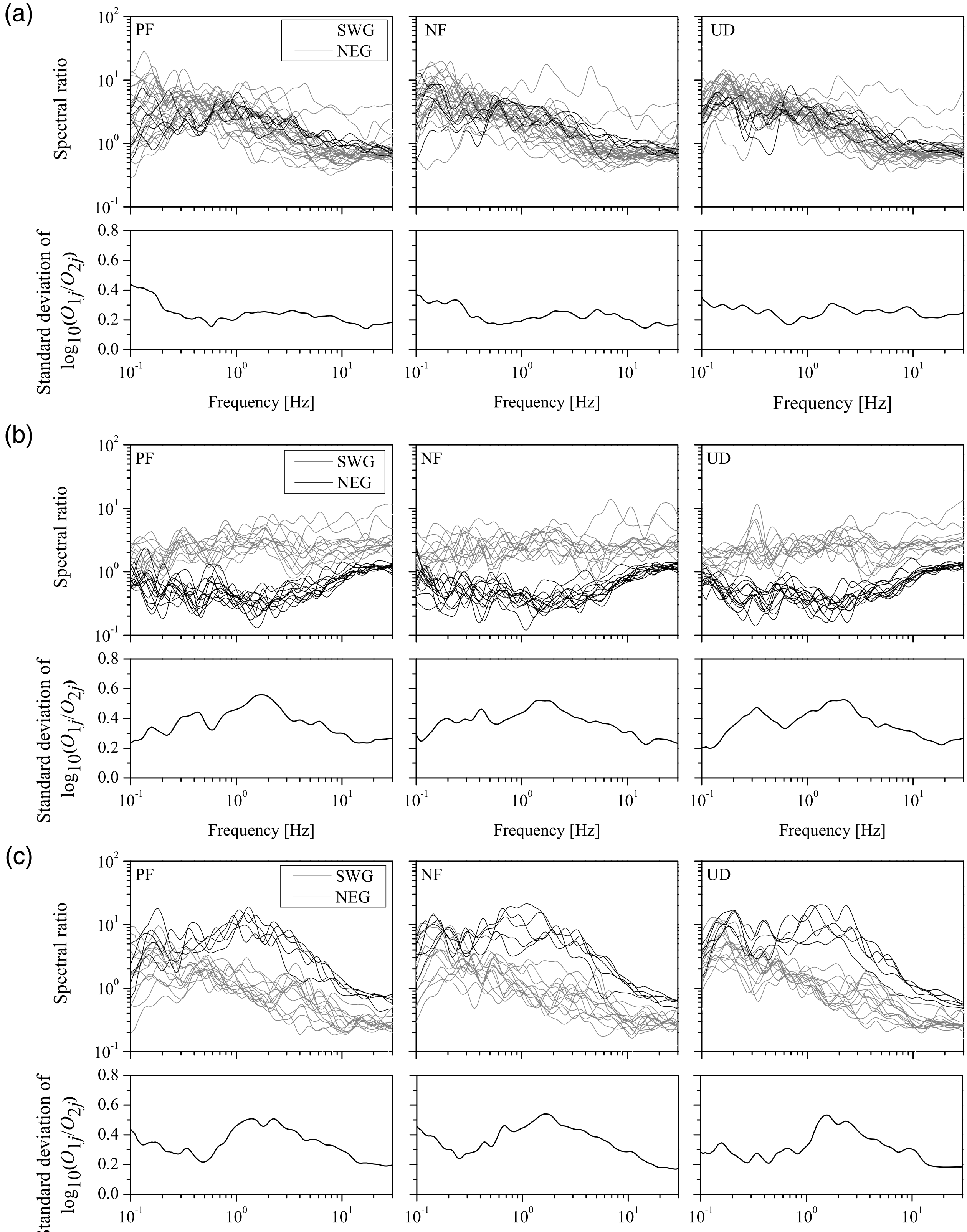

Figure 6. Fourier spectral ratios and standard deviation of $\log_{10}(O_{1j}/O_{2j})$ for (a) the event II/III pair, (b) the event II/IV pair, and (c) the event IV/III pair for the NEG and SWG groups. (PF, strike-parallel; NF, strike-normal; UD, up-down component.)

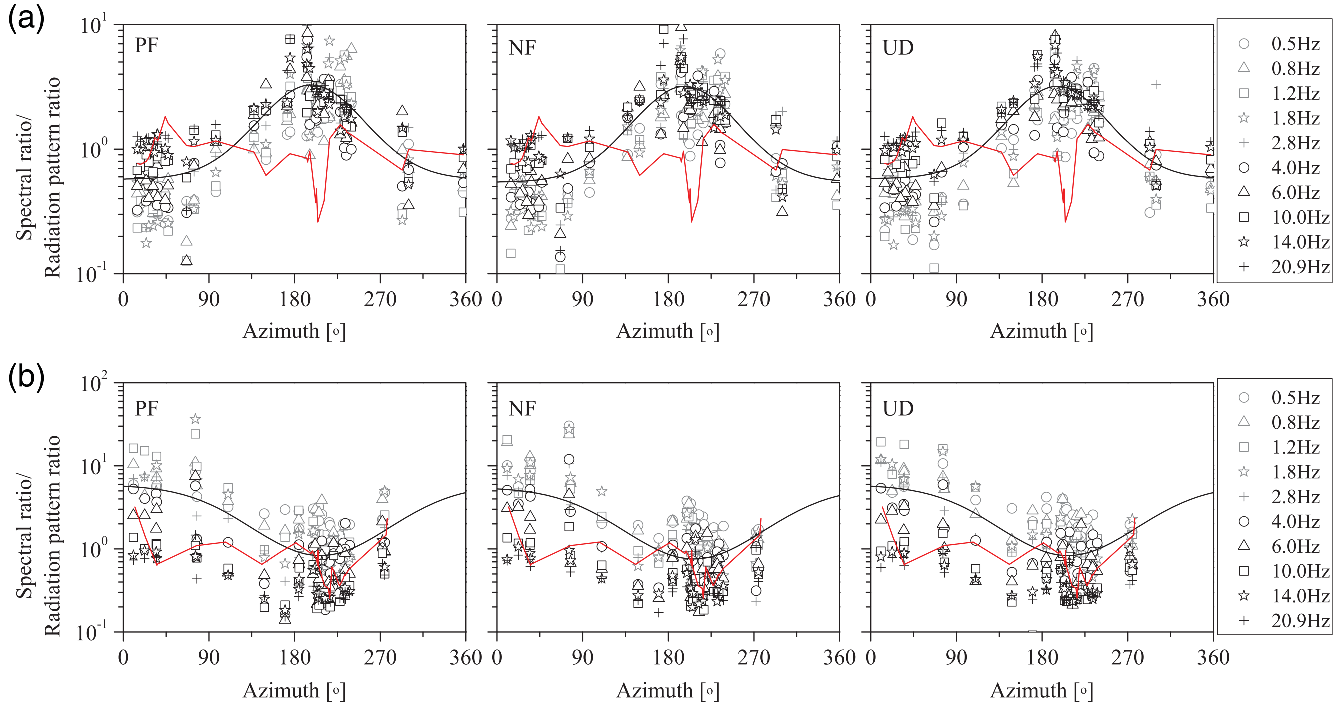

Figure 7. Variations of the spectral ratios with azimuth at some frequencies for (a) the event II/IV pair and (b) the event IV/III pair. The black line represents the best-fit curve to all the points, and the red line represents the radiation pattern ratios. (PF, strike parallel; NF, strike normal; and UD, up-down component.)

pair, while the trough was not visible for the latter. Therefore, we can interpret that the source directivity is mainly ascribed to the source rupture directivity rather than to the radiation pattern.

Inverting Source Rupture Parameters

For a simple homogeneous kinematic line source model that ruptures unilaterally, the rupture directivity can be quantitatively described by the directivity coefficient (Ben-Menahem, 1961),

$$C_d = \frac{1}{1 - (\frac{v_r}{c}) \cos \vartheta}, \tag{2}$$

in which v_r/c is the Mach number (c is the shear-wave velocity, and v_r is the rupture velocity), and ϑ is the angle between the ray that leaves the source and the direction of the rupture propagation (Joyner, 1991).

In fact, sources of most earthquakes have more or less bilateral properties rather than unilateral rupture propagation. A rupture may initiate from any position on the fault plane. If the rupture does not initiate from either end, a single fault can be divided into two subfaults that rupture to the opposite ends. The vector superposition of the directivity coefficients of the two subfaults represents the overall directivity coefficient (Boatwright, 2007; Convertito *et al.*, 2012), which is represented as

$$C_d = \sqrt{\frac{k^2}{[1 - (\frac{v_r}{c}) \cos \vartheta]^2} + \frac{(1-k)^2}{[1 + (\frac{v_r}{c}) \cos \vartheta]^2}}, \tag{3}$$

in which k represents the proportion of rupture in one direction, accounting for the whole rupture, and constrains the predominant rupture direction. If $k > 0.5$, this rupture direction is the predominant rupture direction, otherwise the opposite direction is the predominant one.

Although correction factors have been applied to the ground-motion prediction equation (GMPE) to model the directivity (Spudich *et al.*, 2008), the rupture directivity effect was not included in most of the GMPEs that were derived from regression analyses of large numbers of strong-motion recordings. In theory, the residual between the theoretical predictions and the observed values that are corrected by a coefficient C_d to eliminate the directivity effect reaches a minimum, which is represented as

$$\sum_{i=1}^{N} [\ln(Y_i^{\mathrm{O}}/C_d) - C_i^{\mathrm{un}} \ln Y_i^{\mathrm{P}}]^2 = \min, \tag{4}$$

in which Y_i^O and Y_i^P represent the observed and predicted peak parameters (PGA or PGV) respectively, and N is the number of the strong-motion recordings. The C_i^{un} term is the random variable accounting for uncertainties in source mislocation, radiation pattern, and site effects that may not be properly accounted for by the GMPE. It assumes a Gaussian

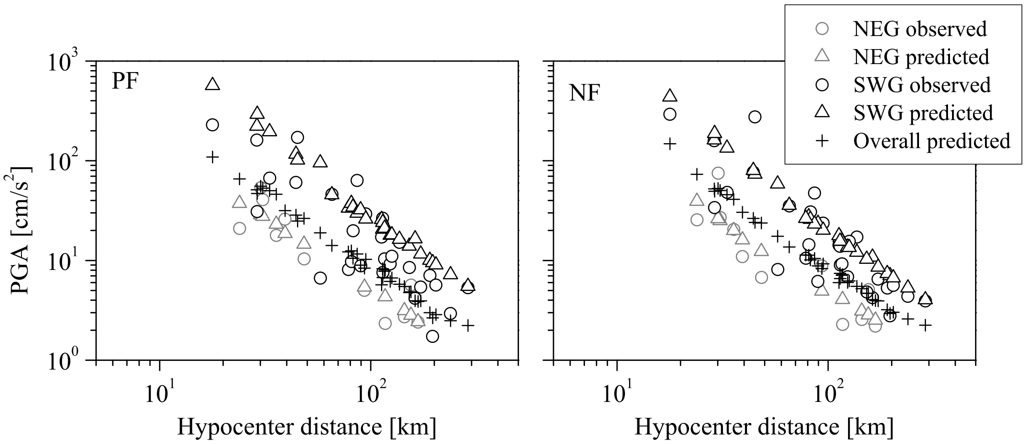

Figure 8. An example of the procedures in which the ground-motion prediction equations (GMPEs) of PGAs of the two horizontal components (PF and NF) were developed for event II. The predicted values were obtained from equation (5) using the regressions from the NEG, SWG, and NEG + SWG recordings. (PF, strike-parallel; NF, strike-normal component.)

distribution with the mean value (μ) of 1.0 and the standard deviation (σ), which is equal to a certain percentage of the standard deviation of the GMPE.

Wen and Ren (2014) compared the observed PGAs and PGVs from the Lushan mainshock with some popular GMPEs in China: Huo89 for southwest China (Huo, 1989), YW06 for western China (Yu and Wang, 2006), Lei07 for the Sichuan basin (Lei *et al.*, 2007), and Yu13 for the fifth-generation Chinese seismic zonation map (Yu *et al.*, 2013). The Huo89 GMPE includes both the rock-site and the soil-site conditions; the other three GMPEs considered only the rock-site condition. An azimuthal site condition will obscure the precise determination of the source rupture directivity. Therefore, we developed a simplified ground-motion model that included both the hypocenter distance R_{hyp} and the site condition V_{S30}, given by

$$\ln(Y) = a + b\ln(c + R_{\mathrm{hyp}}) + d\ln(V_{S30}) + \sigma_{\ln Y}, \quad (5)$$

in which Y represents the observed PGA or PGV and coefficients a, b, c, and d are derived from the regression based on the least-squares method with the standard deviation $\sigma_{\ln Y}$ of the regression.

We introduced the procedures of the development of the GMPE for an event to eliminate the directivity effect as much as possible. First, two GMPEs were separately derived for the NEG and SWG. Then, each strong-motion station that was triggered in the event was given two predicted values using the two GMPEs in the previous step. Finally, a new GMPE was derived from the regression analysis of the geometric average of the two predicted values, which excluded the directivity effect. Figure 8 shows an example of the above-mentioned procedures, in which the GMPE of the PGA was developed for event II. The predicted values of either group match the observed values well, and the overall predicted values also represent the medians of the two groups.

Results and Discussion

Using equation (4), we inverted the peak ground-motion parameters utilizing a grid-searching technique to identify the source rupture parameters, mainly including the predominant rupture direction φ and the rupture velocity v_r. Considering the uncertainty, 500 random realizations of the inversion were made independently in this study to derive 500 groups of optimal source rupture parameters. The random variable C_i^{un} ($i = 1, N$) of each realization, which followed a Gaussian distribution with $\mu = 1.0$ and $\sigma = \sigma_{\ln Y}$, was generated through the Monte Carlo sampling techniques.

The histograms for the optimal source rupture parameters inverted independently by PGA and PGV of the four aftershocks are shown in Figure 9. The mean value and the standard deviation of the results of the inversion are shown in Table 2, and the rupture direction and the proportions in the opposite directions, which were inverted for by PGA and PGV, respectively, are marked in Figure 2. Figure 10 shows the directivity coefficient C_d calculated using equation (3) with the mean values of the source rupture parameters.

Similar results were obtained from both the PGA and PGV inversions. All four events were more likely to rupture on the northeast–southwest-trending fault plane, while it was also possible for event I to rupture the northwest–southwest or north–south-trending fault plane according to the results of inversion of PGA. Fewer strong-motion recordings for event I may be responsible for the much higher uncertainty in the results of inversion than that of other events. For events II, III, and IV, it was verified that the predominant rupture direction (southwest for events II and III and northeast for event IV) agreed well with one of the nodal planes from the Global CMT (Table 1), the orientation of the seismogenic fault, and the alignment of the high-resolution aftershock relocations (Su *et al.*, 2013; Han *et al.*, 2014). The four events shared a similar Mach number, which was approximately 0.6. We calculated a rupture velocity of 2.1 km/s using the 1D

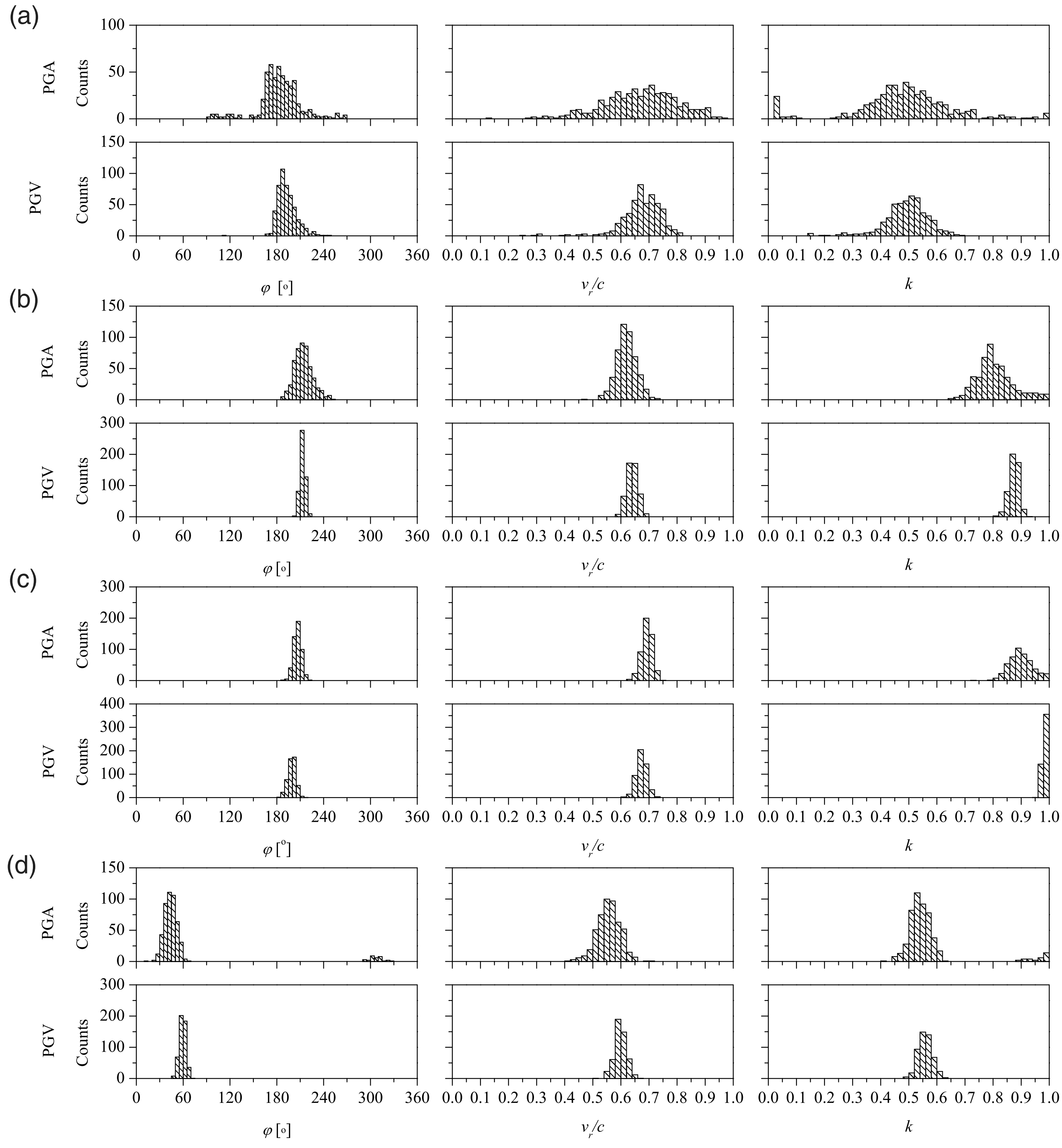

Figure 9. The histograms for the source rupture parameters inverted by PGA and PGV for (a) event I, (b) event II, (c) event III, and (d) event IV. k is the percentage in the rupture direction φ accounting for the whole rupture length.

velocity model of the Longmen Shan region proposed by Zheng *et al.* (2009) ($c = 3.5$ km/s at depths from 2 to 22 km), which is coincident with the rupture velocity of 2.0 m/s of the mainshock that was obtained by Hao *et al.* (2013).

The location of an earthquake along the scale ranging from a perfectly symmetric bilateral rupture to a uniform unilateral rupture can be quantified by the directivity ratio e, which is equal to $2k - 1$. Its absolute value ranges from 0 for a perfectly symmetric bilateral rupture to 1 for a uniform slip unilateral rupture (McGuire, 2004; Boatwright, 2007). For event I, e is approximately equal to 0 but has high uncertainty (0.36 for PGA and 0.16 for PGV). It is not easy to determine whether event I ruptured symmetrically or asymmetrically, though C_d varies slightly around 1.0. Combining the

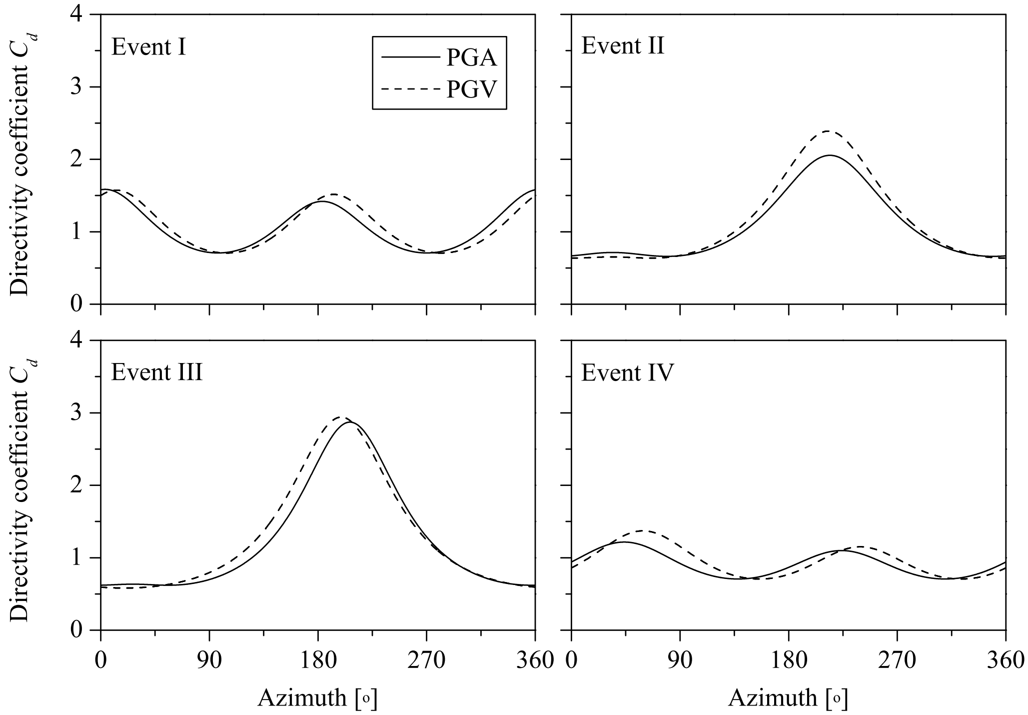

Figure 10. Variation of the directivity coefficients C_d with azimuth inverted for by PGA (solid line) and PGV (dashed line).

strong ground motions characterized by the insignificant directivity effect, we are more likely to consider event I to be an approximately symmetric bilateral rupture. The inversions for events II and III yielded similar severely asymmetric bilateral ruptures, but with approximately 80% of the rupture propagating toward the southwest and 20% toward the northeast for event II and approximately 90% of the rupture propagating toward the southwest and 10% toward the northeast for event III. Event III exhibited a more significant rupture directivity effect, with a forward C_d of 3.0, which is larger than that of event II (2.0). For event IV, the results indicate that the rupture was approximately symmetrically bilateral, slightly inclining to the northeast. C_d varies near 1.0. The rupture propagation approximately consistently contributed to the azimuthal ground motion. Our results can be used to interpret the uneven distribution of the triggered stations and the characteristics of the ground-motion parameters at the azimuthal site locations.

The Lushan earthquake ruptured the southern segment of the LFS in Sichuan, China, and the 2008 Wenchuan earthquake ruptured the north-central segments of the LFS. Zhang *et al.* (2014) and Liu *et al.* (2013) found that there was a 40–50 km central unruptured area between the major slip area of the northeast end of the Lushan earthquake and the southwest end of the 2008 Wenchuan earthquake. High-strength diamictite in Baoxing County, which is located to the north of the epicenter and the central unruptured area, obstructed the continuing rupture (Chen and Xu, 2013). Hao *et al.* (2013)

Table 2
Rupture Parameters of the Four Events That Were Independently Inverted Using PGA and PGV

Event	Peak Parameter	φ	v_r/c	k	e
I	PGA	3.6 ± 27.5	0.66 ± 0.13	0.53 ± 0.18	0.06 ± 0.36
	PGV	12.9 ± 12.5	0.67 ± 0.07	0.51 ± 0.08	0.02 ± 0.16
II	PGA	214.2 ± 11.6	0.61 ± 0.04	0.80 ± 0.07	0.60 ± 0.14
	PGV	212.9 ± 3.3	0.64 ± 0.02	0.86 ± 0.02	0.72 ± 0.04
III	PGA	206.5 ± 5.1	0.69 ± 0.02	0.89 ± 0.04	0.78 ± 0.08
	PGV	199.2 ± 5.2	0.67 ± 0.01	0.97 ± 0.01	0.94 ± 0.02
IV	PGA	43.8 ± 7.7	0.55 ± 0.04	0.53 ± 0.03	0.06 ± 0.06
	PGV	59.2 ± 4.1	0.59 ± 0.02	0.55 ± 0.03	0.10 ± 0.06

PGA, peak ground acceleration; PGV, peak ground velocity; φ, rupture direction; v_r, rupture velocity; c, shear-wave velocity; k, proportion of rupture in one direction; e, directivity ratio.

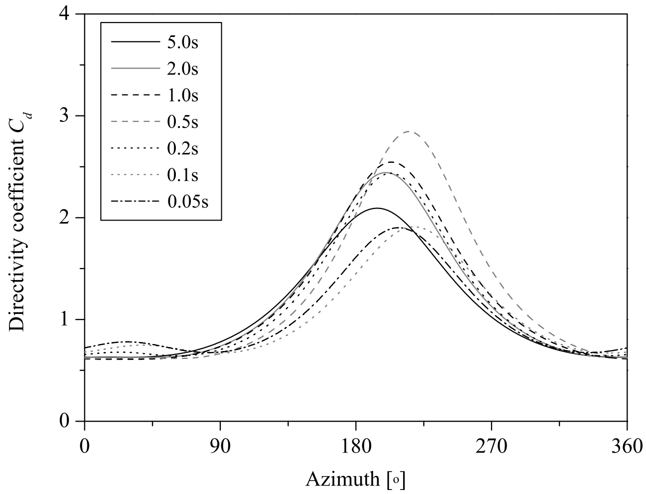

Figure 11. Directivity coefficients C_d inverted for using the PSAs at different periods for event II.

also proposed that the complex faulting activity northeast of the Lushan earthquake might block the further extension of the Lushan coseismic rupture. Our studies showed that Lushan aftershocks could have the tendency to rupture predominantly toward the southwest, which was consistent with the abovementioned studies.

We observed much greater directivity effects at the intermediate periods or frequencies (Figs. 3 and 6). We furthermore inverted the PSAs of event II at periods $T = 5.0$, 2.0, 1.0, 0.5, 0.2, 0.1, and 0.05 s to determine the rupture parameters (Table 3) and the directivity coefficients (Fig. 11) and revealed the period-dependent directivity effect. The results of the inversion yielded a similar predominant rupture direction, which was approximately consistent with those inverted using the PGA and the PGV. A higher C_d was observed at the intermediate periods (~0.5 s), and an obvious period-dependent directivity effect was confirmed, especially in the direction of the predominant rupture. Therefore, the period-dependent directivity effect will inevitably increase the seismic damage of structures.

Conclusions

The dense NSMONS network in this region provided a large number of strong ground motion recordings from the four Lushan aftershocks (events I, II, III, and IV). We divided the strong-motion stations into two groups, the NEG and the SWG, with reference to the epicenter of aftershock and the strike of the mainshock, and compared the ground-motion parameters of the two groups, that is, the peak parameters, PSAs, and durations. The results indicate that events II and III exhibited significant directivity effects in their related ground motions, but such effects were not clearly observed in events I and IV. Furthermore, we took advantage of the Fourier spectral ratio method to imprint the source rupture directivity, which caused the azimuthal ground motions. Finally, an inversion method, based on the analysis of the directivity effect on the peak ground-motion parameters, PGA and PGV, was adopted to determine the predominant rupture direction and rupture velocity through a grid-searching technique. Uncertainties were also considered by a large number of random realizations of the inversions.

Table 3
Rupture Parameters That Were Inverted for Using the Pseudospectral Acceleration (PSA) for Event II

Period (s)	φ	v_r/c	k
5.0	194.1 ± 7.8	0.58 ± 0.03	0.87 ± 0.03
2.0	199.9 ± 3.0	0.64 ± 0.02	0.88 ± 0.02
1.0	203.5 ± 3.3	0.64 ± 0.01	0.91 ± 0.01
0.5	215.2 ± 6.8	0.68 ± 0.02	0.90 ± 0.02
0.2	203.2 ± 13.6	0.65 ± 0.05	0.84 ± 0.07
0.1	218.5 ± 16.9	0.60 ± 0.07	0.77 ± 0.09
0.05	208.3 ± 13.3	0.60 ± 0.04	0.75 ± 0.07

The four events were more likely to share the similar northeast–southwest-trending fault plane, which agrees well with the rupture plane of the mainshock, the orientation of the seismogenic fault, and the distribution of the aftershocks. The four events also shared a similar slower rupture velocity of approximately 2.1 km/s. Allowing for both the characteristics of the strong ground motions and the results of the inversion, event I might be a symmetric bilateral rupture. The results of the inversion for events II and III indicated that the ruptures predominantly propagated toward the southwest, and event III had a more obvious rupture directivity effect, which would dramatically amplify the ground motion in the predominant rupture direction. The rupture propagation of the smaller earthquake is also important. Event IV was verified to be an approximately symmetric bilateral rupture, and the rupture directivity effect was insignificant. However, the percent of the rupture in the northeast was slightly higher than that in the southwest.

Azimuthal variation of the directivity effect was related to the period (Figs. 3 and 6). The results of inversion for PSAs at different periods also confirmed the period-dependent directivity effect. More significant rupture directivity effect could be observed at the intermediate periods (~0.5 s), which was inconsistent with the theoretical idea that rupture directivity mainly affects the higher frequencies. It may be ascribed to a heterogeneous slip process (Bernard *et al.*, 1996). The more obvious rupture directivity effect at intermediate periods will increase the seismic damage.

Data and Resources

All of the strong-motion data that were used in this article can be obtained from the China Strong-Motion Networks Center at www.csmnc.net (last accessed December 2013). The earthquake parameters were obtained from China Earthquake Network Center (CENC; www.csndmc.ac.cn/newweb/data.htm, last accessed December 2013). The Global Centroid

Moment Tensor catalog is available for download at www.globalcmt.org/CMTsearch.html (last accessed January 2014). The V_{S30} measurements for some of the stations were obtained from the Next Generation Attenuation (NGA) site database of the Pacific Earthquake Engineering Research Center and are available for download at http://peer.berkeley.edu/nga/ (last accessed Mach 2014). Some of the plots were produced using Generic Mapping Tools (Wessel and Smith, 1991).

Acknowledgments

We are very grateful to the reviewers for reviewing the manuscript and providing valuable comments. This work is supported by the Nonprofit Industry Research Project of China Earthquake Administration (CEA) under Grant Number 201508005, National Natural Science Fund Numbers 51278473 and 51308515, and Science Fund of Heilongjiang Province Number LC2015022.

References

Ben-Menahem, A. (1961). Radiation of seismic surface-waves from finite moving sources, *Bull. Seismol. Soc. Am.* **51,** 401–435.

Bernard, P., A. Herrero, and C. Berge (1996). Modeling directivity of heterogeneous earthquake ruptures, *Bull. Seismol. Soc. Am.* **86,** 1149–1160.

Boatwright, J. (2007). The persistence of directivity in small earthquakes, *Bull. Seismol. Soc. Am.* **97,** 1850–1861.

Boatwright, J., and D. M. Boore (1982). Analysis of the ground accelerations radiated by the 1980 Livermore Valley earthquakes for directivity and dynamic source characteristics, *Bull. Seismol. Soc. Am.* **72,** 1843–1865.

Bommer, J. J., P. J. Stafford, and J. E. Alarcón (2009). Empirical equations for the prediction of the significant, bracketed, and uniform duration of earthquake ground motion, *Bull. Seismol. Soc. Am.* **99,** 3217–3233.

Boore, D. M. (2001). Effect of baseline corrections on displacements and response spectra for several recordings of the 1999 Chi-Chi, Taiwan, earthquake, *Bull. Seismol. Soc. Am.* **91,** 1199–1211.

Chen, C., and Y. Xu (2013). Relocation of the Lushan M_s 7.0 earthquake sequence and its tectonic implication, *Chin. J. Geophys.* **56,** 4028–4036, doi: 10.6038/cjg20131208 (in Chinese).

Convertito, V., and A. Emolo (2012). Investigating rupture direction for three 2012 moderate earthquakes in northern Italy from inversion of peak ground-motion parameters, *Bull. Seismol. Soc. Am.* **102,** 2761–2770.

Convertito, V., M. Caccavale, R. De Matteis, A. Emolo, D. J. Wald, and A. Zollo (2012). Fault extent estimation for near-real-time ground-shaking map computation purposes, *Bull. Seismol. Soc. Am.* **102,** 661–679.

Han, L. B., X. F. Zeng, C. S. Jiang, S. D. Ni, H. J. Zhang, and F. Long (2014). Focal mechanisms of the 2013 M_w 6.6 Lushan, China earthquake and high-resolution aftershock relocations, *Seismol. Res. Lett.* **85,** 8–14, doi: 10.1785/0220130083.

Hao, J. L., C. Ji, W. M. Wang, and Z. X. Yao (2013). Rupture history of the 2013 M_w 6.6 Lushan earthquake constrained with local strong motion and teleseismic body and surface waves, *Geophys. Res. Lett.* **40,** 5371–5376, doi: 10.1002/2013GL056876.

Hoshiba, M. (2003). Fluctuation of wave amplitude even when assuming convolution of source, path and site factors—Effect of rupture directivity, *Phys. Earth Planet. In.* **137,** 45–65, doi: 10.1016/S0031-9201(03)00007-4.

Hu, J. J., and L. L. Xie (2011). Directivity in the basic parameters of the near-field acceleration ground-motions during the Wenchuan earthquake, *Chin. J. Geophys.* **54,** 2581–2589, doi: 10.3969/j.issn.0001-5733.2011.10.015 (in Chinese).

Huo, J. R. (1989). Study on the attenuation laws of strong earthquake ground motion near the source, *Ph. D. Dissertation*, Institute of Engineering Mechanics, China Earthquake Administration, Harbin, China (in Chinese).

Joyner, W. B. (1991). Directivity for non-uniform ruptures, *Bull. Seismol. Soc. Am.* **81,** 1391–1395.

Kane, D. L., P. M. Shear, B. P. Goertz-Allmann, and F. L. Vernon (2013). Rupture directivity of small earthquakes at Parkfield, *J. Geophys. Res.* **118,** 1–10, doi: 10.1029/2012JB009675.

Lanza, V., D. Spallarossa, M. Cattaneo, D. Bindi, and P. Augliera (1999). Source parameters of small events using constrained deconvolution with empirical Green's functions, *Geophys. J. Int.* **137,** 651–662.

Lei, J. C., M. T. Gao, and Y. X. Yu (2007). Seismic motion attenuation relations in Sichuan and adjacent areas, *Acta. Seismol. Sinica* **29,** 500–511 (in Chinese).

Li, X. J., Z. H. Zhou, H. Y. Yu, R. Z. Wen, D. W. Lu, and M. Huang (2008). Strong motion observation and recordings from the great Wenchuan earthquake, *Earth Eng. Eng. Vib.* **7,** 235–246.

Liu, J., G. X. Yi, Z. W. Zhang, Z. J. Guan, X. Luan, F. Long, and F. Du (2013). Introduction to the Lushan, Sichuan M 7.0 earthquake on 20 April 2013, *Chin. J. Geophys.* **56,** 1404–1407 (in Chinese).

López-Comino, J.-Á., F. de Lis Mancilla, J. Morales, and D. Stich (2012). Rupture directivity of the 2011, M_w 5.2 Lorca earthquake (Spain), *Geophys. Res. Lett.* **39,** L03301, doi: 10.1029/2011GL050498.

Ma, H. S., S. Y. Wang, S. P. Pei, J. Liu, W. Hua, and L. Q. Zhou (2007). Q_0 tomography of S wave attenuation in Sichuan-Yunnan and adjacent regions, *Chin. J. Geophys.* **50,** 465–471 (in Chinese).

Matheron, G. (1973). The intrinsic random functions and their applications, *Adv. Appl. Prob.* **5,** 439–468.

McGuire, J. J. (2004). Estimating finite source properties of small earthquake ruptures, *Bull. Seismol. Soc. Am.* **94,** 377–393.

McGuire, J. J., L. Zhao, and T. H. Jordan (2002). Predominance of unilateral rupture for a global catalog of large earthquakes, *Bull. Seismol. Soc. Am.* **92,** 3309–3317.

Mori, J. (1996). Rupture directivity and slip distribution of the M 4.3 foreshock to the 1992 Joshua Tree earthquake, southern California, *Bull. Seismol. Soc. Am.* **86,** 805–810.

Phung, V., G. M. Atkinson, and D. T. Lau (2004). Characterization of directivity effects observed during 1999 Chi-Chi, Taiwan earthquake, *13th World Conference of Earthquake Engineering*, Vancouver, B.C., Canada, 1–6 August 2004.

Ren, Y. F., R. Z. Wen, and B. F. Zhou (2011). Cataloging strong-motion recordings—An example of Wenchuan mobile strong-motion observation, *Technol. Earthq. Disaster Prev.* **6,** 406–415 (in Chinese).

Seekins, L. C., and J. Boatwright (2010). Rupture directivity of moderate earthquakes in northern California, *Bull. Seismol. Soc. Am.* **100,** 1107–1119.

Somerville, P., K. Irikura, R. Graves, S. Sawada, D. Wald, N. Abrahamson, Y. Iwasaki, T. Kagawa, N. Smith, and A. Kowada (1999). Characterizing crustal earthquake slip models for the prediction of strong ground motion, *Seismol. Res. Lett.* **70,** 59–80.

Somerville, P. G., R. W. Graves, and N. F. Smith (1996). Forward rupture directivity in the Kobe and Northridge earthquakes, and implications for structural engineering, *Seismol. Res. Lett.* **67,** 55.

Spudich, P., M. Eeri, and B. S. J. Chiou (2008). Directivity in NGA earthquake ground motions: Analysis using isochrones theory, *Earthq. Spectra* **24,** 279–298.

Su, J. R., Y. Zheng, J. S. Yang, T. C. Chen, and Q. Wu (2013). Accurate locating of the Lushan, Sichuan M 7.0 earthquake on 20 April 2013 and its aftershocks and analysis of the seismogenic structure, *Chin. J. Geophys.* **56,** 2634–2644 (in Chinese).

Tan, Y., and D. Helmberger (2010). Rupture directivity characteristics of the 2003 Big Bear sequence, *Bull. Seismol. Soc. Am.* **100,** 1089–1106.

Velasco, A. A., C. J. Ammon, and T. Lay (1994). Empirical Green function deconvolution of broadband surface waves: Rupture directivity of the 1992 Landers, California ($M_w = 7.3$), earthquake, *Bull. Seismol. Soc. Am.* **84,** 735–750.

Wang, S. Y., S. P. Pei, M. H. Thomas, Z. H. Xu, F. N. James, and Y. X. Yu (2008). Crustal S-wave Q estimated from M_L amplitude II: Q lateral variation in China, *Chin. J. Geophys.* **51,** 133–139 (in Chinese).

Wang, W. M., J. L. Hao, and Z. X. Yao (2013). Preliminary result for rupture process of Apr. 20, 2013, Lushan earthquake, Sichuan, China, *Chin. J. Geophys.* **56,** 1412–1417, doi: 10.6038/cjg20130436 (in Chinese).

Wen, R. Z., and Y. F. Ren (2014). Strong-motion observations of the Lushan earthquake on 20 April 2013, *Seismol. Res. Lett.* **85,** 1043–1055, doi: 10.1785/0220140006.

Wessel, P., and W. H. F. Smith (1991). Free software helps map and display data, *Eos Trans. AGU* **72,** 441.

Yu, Y. X., and S. Y. Wang (2006). Attenuation relations for horizontal peak ground motion acceleration and response spectrum in eastern and western China, *Technol. Earthq. Disaster Prev.* **1,** 206–217 (in Chinese).

Yu, Y. X., S. Y. Li, and L. Xiao (2013). Development of ground motion attenuation relations for the new seismic hazard map of China, *Technol. Earthq. Disaster Prev.* **8,** 24–33 (in Chinese).

Zhang, G. W., and J. S. Lei (2013). Relocation of Lushan, Sichuan strong earthquake (M_S 7.0) and its aftershocks, *Chin. J. Geophys.* **56,** 1764–1771, doi: 10.6038/cjg20130534 (in Chinese).

Zhang, Y., R. J. Wang, Y. T. Chen, L. S. Xu, F. Du, M. P. Jin, H. W. Tu, and T. Dahm (2014). Kinematic rupture model and hypocenter relocation of the 2013 M_W 6.6 Lushan earthquake constrained by strong-motion and teleseismic data, *Seismol. Res. Lett.* **85,** 15–22, doi: 10.1785/0220130126.

Zhang, Y., L. S. Xu, and Y. T. Chen (2013). Rupture process of the Lushan 4.20 earthquake and preliminary analysis on the disaster-causing mechanism, *Chin. J. Geophys.* **56,** 1408–1411, doi: 10.6038/cjg20130435 (in Chinese).

Zheng, Y., H. S. Ma, J. Lyu, S. D. Ni, Y. C. Li, and S. J. Wei (2009). Source mechanism of strong aftershocks ($M_S \geq 5.6$) of the 2008/05/12 Wenchuan earthquake and the implication for seismotectonics, *Sci. China Ser. D.* **52,** 739–753.

Institute of Engineering Mechanics
China Earthquake Administration
Key Laboratory of Earthquake Engineering and Engineering Vibration of China Earthquake Administration
No. 29 Xuefu Road
Harbin, China
ruizhi@iem.ac.cn
whw1990413@163.com
renyefei@iem.ac.cn

Manuscript received 15 September 2015;
Published Online 10 November 2015